Comprehensive investigation of lateral dose profile and output factor measurements in small proton fields from different delivery techniques

Kretschmer, Jana; Brodbek, Leonie; Behrends, Carina; Kugel, Fabian; Koska, Benjamin; Bäumer, Christian; Wulff, Jörg; Timmermann, Beate; Poppe, Björn; Looe, Hui Khee

Published in:
Medical Physics

DOI:
10.1002/mp.16357

Received: 6 September 2022 | Revised: 22 February 2023 | Accepted: 24 February 2023

DOI: 10.1002/mp.16357

RESEARCH ARTICLE

MEDICAL PHYSICS

Comprehensive investigation of lateral dose profile and output factor measurements in small proton fields from different delivery techniques

Jana Kretschmer[1,2] | **Leonie Brodbek**[1,2,3] | **Carina Behrends**[4,5,6] | **Fabian Kugel**[4,5,7] | **Benjamin Koska**[4,5] | **Christian Bäumer**[4,5,6,8] | **Jörg Wulff**[4,5] | **Beate Timmermann**[4,5,8,9] | **Björn Poppe**[1] | **Hui Khee Looe**[1]

[1]University Clinic for Medical Radiation Physics, Medical Campus Pius Hospital, Carl-von-Ossietzky University Oldenburg, Oldenburg, Germany

[2]Department of Radiation Oncology, University Medical Center Groningen, University of Groningen, Groningen, The Netherlands

[3]EBG MedAustron GmbH, Wiener Neustadt, Austria

[4]West German Proton Therapy Centre Essen, Essen, Germany

[5]West German Cancer Center (WTZ), Essen, Germany

[6]Department of Physics, TU Dortmund University, Dortmund, Germany

[7]Department of Physics, Heinrich-Heine University, Düsseldorf, Germany

[8]German Cancer Consortium (DKTK), Heidelberg, Germany

[9]University Hospital Essen, Essen, Germany

Correspondence
Jana Kretschmer, University Clinic for Medical Radiation Physics, Medical Campus Pius Hospital, Carl-von-Ossietzky University Oldenburg, Oldenburg 26129, Germany.
Email: jana.kretschmer@uni-oldenburg.de

Funding information
DFG, Grant/Award Number: INST 184/157-1 FUGG

Abstract

Background and purpose: As a part of the commissioning and quality assurance in proton beam therapy, lateral dose profiles and output factors have to be acquired. Such measurements can be performed with point detectors and are especially challenging in small fields or steep lateral penumbra regions as the detector's volume effect may lead to perturbations. To address this issue, this work aims to quantify and correct for such perturbations of six point detectors in small proton fields created via three different delivery techniques.

Methods: Lateral dose profile and output measurements of three proton beam delivery techniques (pencil beam scanning, pencil beam scanning combined with collimators, passive scattering with collimators) were performed using high-resolution EBT3 films, a PinPoint 3D 31022 ionization chamber, a microSilicon diode 60023 and a microDiamond detector 60019 (all PTW Freiburg, Germany). Detector specific lateral dose response functions $K(x,y)$ acting as the convolution kernel transforming the undisturbed dose distribution $D(x,y)$ into the measured signal profiles $M(x,y)$ were applied to quantify perturbations of the six investigated detectors in the proton fields and correct the measurements. A signal theoretical analysis in Fourier space of the dose distributions and detector's $K(x,y)$ was performed to aid the understanding of the measurement process with regard to the combination of detector choice and delivery technique.

Results: Quantification of the lateral penumbra broadening and signal reduction at the fields center revealed that measurements in the pencil beam scanning fields are only compromised slightly even by large volume ionization chambers with maximum differences in the lateral penumbra of 0.25 mm and 4% signal reduction at the field center. In contrast, radiation techniques with collimation are not accurately represented by the investigated detectors as indicated by a penumbra broadening up to 1.6 mm for passive scattering with collimators and 2.2 mm for pencil beam scanning with collimators. For a 3 mm diameter collimator field, a signal reduction at field center between 7.6% and 60.7% was asserted. Lateral dose profile measurements have been corrected via deconvolution with the corresponding $K(x,y)$ to obtain the undisturbed $D(x,y)$. Corrected output ratios of the passively scattered collimated fields obtained for

the microDiamond, microSilicon and PinPoint 3D show agreement better than 0.9% (one standard deviation) for the smallest field size of 3 mm.
Conclusion: Point detector perturbations in small proton fields created with three delivery techniques were quantified and found to be especially pronounced for collimated small proton fields with steep dose gradients. Among all investigated detectors, the microSilicon diode showed the smallest perturbations. The correction strategies based on detector's $K(x,y)$ were found suitable for obtaining unperturbed lateral dose profiles and output factors. Approximation of $K(x,y)$ by considering only the geometrical averaging effect has been shown to provide reasonable prediction of the detector's volume effect. The findings of this work may be used to guide the choice of point detectors in various proton fields and to contribute toward the development of a code of practice for small field proton dosimetry.

KEYWORDS
lateral penumbra, output factors, proton fields, small field dosimetry, volume effect

1 | INTRODUCTION

Dosimetry of small or steep radiation fields can be challenging and recent works have emphasized the need for higher spatial accuracy of detectors in proton therapy[1] as well as investigations of small proton field dosimetry.[2–4] While the dosimetry of small photon fields has been studied intensively in the past and international guidelines were published as a report by the AAPM Task Group 155[5] and as TRS 483 by the IAEA,[6] there are no national or international standards for dosimetry of small proton fields which may require a separate treatment due to the different nature of dose deposition processes of protons from that of photons.

Nevertheless, the commissioning and quality assurance tasks involved are similar to photon beams including measurements of lateral dose profiles and output or field size factors, that is, the change of the dose per monitor unit as a function of field size.[7–9] Such measurements are usually acquired using point detectors with extended sensitive volume that may be subject to perturbations[1,2,10–12] related to the so-called volume effect.[13,14] Although several studies found that the detector's volume effect does not noteworthy perturb measurements of proton fields with Gaussian shaped profiles or large fields with broad lateral penumbra as, for example, occurring in pencil beam scanning (PBS) fields,[13,15–17] volume effect perturbations have been identified in some studies and especially for proton beam delivery techniques leading to reduced penumbras.[1,2,10,12] While small proton fields are used in ocular treatments, treatments of pediatric patients, minibeam irradiations or stereotactic treatments,[4,10,18–20] the smallest possible lateral penumbra is generally desired as this allows for better sparing of adjacent organs at risk.[20–23] As a consequence, several studies presented novel proton irradiation techniques utilizing small proton fields with reduced lateral penumbras.[9,22,24–28]

The anticipated increasing use of small and collimated proton fields motivates further investigations of the performance of detectors under these conditions. The detector's volume effect, being dominant in small fields, may lead to a broadening of the measured lateral penumbra or, during output factor measurements, to a reduction of the measured signal at the field center.[13]

Therefore, correction strategies may be needed for these measurements.[29] One of these is based on the mathematical model in Equation 1, where the volume effect is characterized by the detector specific lateral dose response function $K(x,y)$, which acts as the convolution kernel transforming the undisturbed dose distribution $D(x,y)$ into the measured dose distribution $M(x,y)$ representing the distribution of the background-subtracted electrical signal measured with a detector.[13,30–32]

$$M(x,y) = D(x,y) * K(x,y) \quad (1)$$

Equation 1 also shows that the knowledge of detector specific $K(x,y)$ allows the correction of the measurements performed with the detector, that is, the detector signal with respect to position, $M(x,y)$, to obtain the unperturbed dose distributions $D(x,y)$ by deconvolution. The function $K(x,y)$ encompasses the detector perturbation due to geometrical volume averaging and disturbances of the local particle fluence by non-water equivalent detector components, where the latter is often called the density perturbation in the literature.[14,30,32,33] In the following, the combined effect is referred to as the volume effect.

Recently, Kretschmer et al.[14] investigated the volume effect of point detectors in proton fields and presented one-dimensional $K(x)$ measured in a 150 MeV proton slit beam for various detectors, including ionization chambers and diode-type detectors. The results indicated that $K(x)$ in proton fields can be generally considered as energy and depth independent. Using the knowledge of

the detector specific $K(x,y)$, volume effect perturbation at each position (x,y) in the measured lateral profiles $M(x,y)$ can be quantified according to Equation 1 and corrected to obtain the undisturbed dose profiles $D(x,y)$ by deconvolution techniques.[34] Furthermore, field size dependent output correction factors can be derived.[35]

The aim of this work is to provide insights on small field proton dosimetry by investigating perturbation effects of point detectors with regard to various proton beam delivery techniques. To do so, measurements have been performed with proton fields created via *PBS*, PBS combined with collimators (*collimated PBS*) and passive scattering with collimators (*passively scattered collimated*) using high-resolution EBT3 films, a small volume ionization chamber, a diode, and a diamond detector. Based on the mathematical convolution model (Equation 1) and two-dimensional $K(x,y)$, perturbation effects in the studied proton fields have been quantified separately for each delivery technique. Additionally, signal theoretical analysis has been carried out to compare the undisturbed dose distributions delivered by the three techniques. The differences are discussed in conjunction with the detector specific $K(x,y)$ with regard to the magnitude of perturbations or potential errors, from which the suitability of a detector used for the characterization of small proton fields in each investigated case will be examined.

2 | MATERIALS AND METHODS

2.1 | Beam delivery techniques for small proton fields

The perturbation of point detectors was studied in small proton fields delivered with the three techniques *PBS*, *collimated PBS* and *passively scattered collimated* (see Section 1). All fields were provided using an IBA ProteusPlus system (IBA, Louvain-la-Neuve/Belgium) at the West German Proton Therapy Centre Essen (WPE). In the following, the technical details of each beam delivery technique in conjunction to the measurements performed are elaborated.

2.1.1 | Pencil beam scanning

For the *PBS* delivery technique, monoenergetic proton pencil beams of 160 MeV protons with constant spot weight and 2.5 mm spot spacing were used to generate 10 mm × 10 mm and 20 mm × 20 mm square fields. The underlying pencil beam has a Gaussian distribution free in air at isocenter defined by a standard deviation of 5.1 mm. No range shifters were used. The two-dimensional dose distributions $D(x,y)$ of the fields were measured with Gafchromic EBT3 films (Ashland Speciality Ingredients G.P., Bridgewater, New Jersey, USA), which have been calibrated following the methods described in Brodbek et al.[13] For each field size, three films were positioned in an RW3 solid water phantom (SP34 phantom, IBA Dosimetry, Schwarzenbruck) at 3 cm water equivalent depth at isocenter and irradiated simultaneously. The films were scanned with an Epson 10000XL flatbed scanner (Seiko Epson Corp., Suwa, Japan) at a resolution of 600 dpi and 48 bit. Each film scan was post-processed by applying a 2 mm × 2 mm median filter in MATLAB R2019b.[36] Subsequently, all three films for each field size were aligned and the average was computed.

2.1.2 | Collimated PBS proton fields

For the *collimated PBS* technique, PBS fields were collimated allowing for steeper lateral dose fall-offs. Measurements were performed using a monoenergetic 160 MeV proton field collimated by 6.6 cm thick circular brass collimators of 5, 10, and 15 mm diameter. The PBS fields were delivered without a range shifter. Two-dimensional $D(x,y)$ profiles were determined from EBT3 film measurements using the same methodology as described in Section 2.1.1 with a 0.3 mm × 0.3 mm median filter.

2.1.3 | Passively scattered collimated proton fields

Measurements in *passively scattered collimated* proton fields were carried out at the WPE eye treatment nozzle. An 82.5 MeV proton beam is scattered laterally by tantalum foils and modulated in depth with a spinning modulator wheel. The basic design of the eye nozzle has been described in Slopsema et al.[37] A spread-out-Bragg peak with 25 mm range and 20 mm modulation was selected for measurements, representing a typical radiation field in ocular proton therapy.

Measurements were performed for 12 mm thick collimators with opening diameters of 3, 5, 10, 15, 20, and 30 mm. Lateral profiles $M(x,y = 0)$ and $M(x = 0,y)$ of these fields were measured with a microSilicon diode 60023 and a PinPoint 3D 31022 chamber. In addition, the field outputs at the field center, that is, $M(x = 0,y = 0)$, were measured using the microSilicon, PinPoint 3D and microDiamond 60019. The detectors were connected to a TANDEM electrometer (PTW Freiburg, Germany) and positioned axially under consideration of their effective point of measurement at 15 mm depth in a MP3XS phantom (PTW Freiburg, Germany) with a modified thin entrance window. The phantom's surface was positioned at the isocenter. Lateral profiles of the 5 mm field were scanned along the crossplane (x) and inplane (y) direction to center the detectors for output measurements.

2.2 | Derivation of two-dimensional lateral dose response functions $K(x,y)$

The one-dimensional $K(x)$ for three ionization chambers: a Semiflex 3D 31021 and a PinPoint 3D 31022 (PTW Freiburg, Germany), and a CC01G Razor chamber (IBA Dosimetry, Schwarzenbruck, Germany), a microSilicon diode 60023 and a microDiamond detector 60019 (PTW Freiburg, Germany) have been previously reported in Kretschmer et al.[14] for the axial orientation, that is, the detector's axis is parallel to the beam's axis. Additionally, Monte Carlo simulations in GATE9.0/Geant4.10.06.p03[38,39] were performed in this work according to the methods reported in Kretschmer et al.[14] to determine $K(x)$ for an Advanced Markus 34045 ionization chamber (PTW Freiburg, Germany) not included in the previous work. These functions derived using a narrow slit beam geometry are also referred to as the line spread function. The sought two-dimensional function $K(x,y)$ in Equation 1 or the point spread function is related to the one-dimensional $K(x)$ according to the integral Equation:

$$K(x) = \int_{-\infty}^{+\infty} K(x, y)\ dy \tag{2}$$

By utilizing the rotational symmetry of all investigated detectors around the detector's axis, the corresponding rotational symmetric point spread functions $K(r)$ were calculated from the one-dimensional $K(x)$ by solving an integral Equation, as proposed by Marchand[40] where $r = (x^2 + y^2)^{1/2}$ is the radial distance with origin at the detector's center, that is, point of symmetry. Subsequently, the two-dimensional $K(x,y)$ function was generated with 0.1 mm resolution for each detector from the derived $K(r)$.

2.3 | Application of $K(x,y)$ functions

According to Equation 1, the $K(x,y)$ determined according to the methods presented in Section 2.2 can be used to retrieve the unperturbed dose profile $D(x,y)$ from the measured profile $M(x,y)$ by deconvolution or vice versa by convolution. Since it has been shown that the underlying $K(x)$ are depth and energy independent,[14] the functions are regarded to be shift-invariant and therefore applicable at all previously described radiation fields.

For the *PBS* and *collimated PBS* fields, the undisturbed dose distributions $D(x,y)$ acquired using EBT3 films were compared to the detector signal profiles $M(x,y)$ representing the expected distribution of the background-subtracted electrical signal measured with a detector. The latter was computed from the $D(x,y)$ by application of Equation 1 using the corresponding detector specific $K(x,y)$. The detector's volume effect perturbation was quantified in terms of lateral penumbra broadening and the reduction of the measured signal at the field center with respect to the actual dose at the field center $D(x,y)$. The broadening was defined as the change in the 80%–20% lateral dose fall-off, $\Delta d_{80/20} = d_{80/20,M(x)} - d_{80/20,D(x)}$.[8] The reduction of the measured signal at the field center, also referred to as difference at (0,0) in percent in the following, is defined as $(M(0,0)\text{-}D(0,0))\bullet 100$.

For the *passively scattered collimated* proton fields, the undisturbed dose profile $D(x,y)$ was derived from the measured signal profiles $M(x,y)$ acquired with a microSilicon detector and a PinPoint 3D chamber by deconvolution (Equation 1) utilizing the known detector specific $K(x,y)$. To do so, two-dimensional $M(x,y)$ distributions were computed from the measured profiles along the x- and y-axis, $M(x,y=0)$ and $M(x=0,y)$, respectively, acquired with step sizes in the range of 0.2–0.3 mm. Both profiles were then interpolated to 0.1 mm resolution using a spline interpolation in MATLAB R2019b.[36] A radial symmetrical profile $M_{sym}(r)$ was determined by averaging the four half measured profiles centered at $x = 0$ and $y = 0$. Finally, a two-dimensional $M(x,y)$ distribution with 0.1 mm resolution was generated from the $M_{sym}(r)$. The deconvolution of $M(x,y)$ was performed in two-dimensional space according to an iterative deconvolution approach[41] as described in Looe *et al*.[33] using the two-dimensional lateral dose response functions $K(x,y)$ to obtain the $D(x,y)$ profiles. The iteration was terminated after five iteration cycles to suppress noise amplification.

Furthermore, the detector specific field output correction factors k were calculated according to Equation 3[35] from the measured $M(x = 0, y = 0)$ and the derived $D(x = 0, y = 0)$ of the *passively scattered collimated* fields. The detector output ratio measurements acquired with the microSilicon, PinPoint 3D and microDiamond 60019 were then corrected by multiplication with the derived k factors to obtain the field output factors, that is, the unperturbed relative dose at the field center.

$$k = \frac{D(x = 0, y = 0)}{M(x = 0, y = 0)} \tag{3}$$

2.4 | Application of approximated $K_{area}(x,y)$

As pointed out in Kretschmer et al.,[14] the dominant detector perturbation in small proton fields is attributed to the geometrical volume averaging. Therefore, it is worthwhile to investigate the suitability to approximate the lateral dose response function by a geometrical weighting function as suggested for small photon fields

in TRS-483[6] or by a Gaussian or parabolic function as performed in previous studies to correct proton *PBS* measurements.[15,16] This has been performed using the smallest fields of the three delivery techniques as examples. The rotational symmetrical approximations $K_{area}(r)$ were defined according to a Heaviside function under consideration of the radius of the sensitive area $r_{sensitvieArea}$ (Equation 4). The $d_{80/20}$ and the signal reduction at the maximum have been calculated using $K_{area}(x,y)$ and were compared to the corresponding results obtained from $K(x,y)$.

$$K_{area}(r) = \begin{cases} 1 & for\ r \le r_{sensitiveArea} \\ 0 & for\ r > r_{sensitiveArea} \end{cases} \quad (4)$$

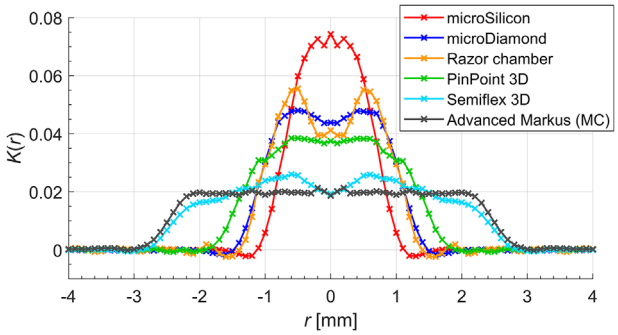

FIGURE 1 Rotationally symmetrical area normalized $K(r)$ of the six investigated point detectors. [Color figure can be viewed at wileyonlinelibrary.com]

2.5 | Signal theoretical anaylsis

The convolution operation described in Equation 1 can be expressed in the Fourier space as multiplication according to Equation 5.

$$FT[M(x,y)] = FT[D(x,y)] \cdot FT[K(x,y)] \quad (5)$$

Based on this relationship, the suitability of a detector associated with a lateral dose response function $K(x,y)$ to characterize an underlying dose distribution $D(x,y)$ can be further evaluated by examining the frequency components in $D(x,y)$ and $K(x,y)$.[13,30,42,43] To do so, the Fourier transform of the narrowest dose profile, that is, the dose profile with smallest lateral width, FT[$D(x,y)$], from each delivery technique was computed and compared to FT[$K(x,y)$] of four selected detectors (microSilicon, PinPoint 3D, Semiflex 3D and Advanced Markus).

2.6 | Influence of detector positioning errors

In addition to perturbations from the detector's volume effect, the detector positioning also plays an important role during output measurements in small fields.[4,10,44] The $M(x,y)$ and $D(x,y)$ determined for the various delivery techniques allow to estimate the impact due to uncertainties in detector positioning. To do so, a selection of proton fields from the investigated delivery techniques: 3, 5, and 10 mm passively scattered collimated fields, 5 and 10 mm collimated PBS fields and a 10 mm x 10 mm PBS field, were analyzed exemplarily by simulating positioning errors up to 1.5 mm. Thereby, the percentage signal reduction in the $M(x,y=0)$ with respect to the corresponding $M(0,0)$ was determined as the values $(1 - \frac{M(x,y=0)}{M(x=0,y=0)}) \cdot 100$ at different off-axis positions x.

3 | RESULTS

3.1 | Two-dimensional lateral dose response functions

Figure 1 shows the rotational symmetrical $K(r)$ for the six point detectors derived from the corresponding $K(x)$ determined experimentally in Kretschmer et al.[14] or simulated in this work (Advanced Markus chamber). The width of $K(r)$ increases with increasing diameter of the sensitive volume such that the Advanced Markus chamber has the broadest function, while the $K(r)$ of the smallest microSilicon diode is the narrowest among the investigated detectors.

3.2 | Pencil beam scanning

Figure 2 shows the measured lateral dose profiles along the x-axis $D(x,y=0)$ as determined from film measurements of the two *PBS* fields with square field sizes of 10 mm (left) and 20 mm (right) side length. The average $d_{80/20}$ of the fields are 6.9 and 8.7 mm, for the 10 mm × 10 mm and 20 mm × 20 mm, respectively. In addition to the $D(x,y=0)$, Figure 2 shows the calculated signal profiles $M(x,y=0)$ for various detectors from the two-dimensional convolution of $D(x,y)$ with the $K(x,y)$ according to Equation 1. For the 10 mm × 10 mm field (left panel), a reduction of the signal maximum of 2.9% (Semiflex 3D) and 4% (Advanced Markus) can be observed. For the 20 mm × 20 mm field (right panel in Figure 2), the $D(x,y=0)$ and all $M(x,y=0)$, show minimal differences along the whole profile. Even for the Advanced Markus chamber the signal reduction at the field center is well below 1.5%. The differences in $d_{80/20}$ of the $M(x,y=0)$ as well as the percentage signal reduction at the field center in the measurements $M(0,0)$ with respect to the undisturbed dose profiles are listed in Table 1.

TABLE 1 Penumbra broadening ($\Delta d_{80/20}$) and reduction of the signal at the field center (0,0) for point detectors in dependence of the field size and investigated delivery technique. $\Delta d_{80/20}$ represents the increase in lateral penumbra calculated as the difference between the $d_{80/20}$ of $M(x,y = 0)$ and that of the corresponding $D(x,y = 0)$. The difference at (0,0) is the percentage signal reduction between the respective $M(0,0)$ and $D(0,0)$. The dose profiles used to retrieve the data are shown in Figure 2 (*PBS*), Figure 3 (*collimated PBS*) and Figure 6 (*passively scattered collimated*)

	PBS - Square field side length [mm]							
	3	**5**	**10**		**15**		**20**	
Detector			**$\Delta d_{80/20}$ [mm]**	**Diff. at (0,0) [%]**			**$\Delta d_{80/20}$ [mm]**	**Diff. at (0,0) [%]**
microSilicon			0.03	−0.34			0.02	−0.13
microDiamond			0.06	−0.68			0.04	−0.27
Razor chamber			0.06	−0.78			0.04	−0.29
PinPoint 3D			0.10	−1.15			0.06	−0.43
Semiflex 3D			0.20	−2.93			0.15	−1.01
Adv. Markus			0.25	−4.00			0.22	−1.34
	Collimated PBS - Aperture diameter [mm]							
	3	**5**	**10**		**15**		**20**	
Detector		**$\Delta d_{80/20}$ [mm]**	**Diff. at (0,0) [%]**	**$\Delta d_{80/20}$ [mm]**	**Diff. at (0,0) [%]**	**$\Delta d_{80/20}$ [mm]**	**Diff. at (0,0) [%]**	
microSilicon		0.30	0.27	0.35	0.15	0.34	−0.98	
microDiamond		0.58	0.12	0.65	0.17	0.62	−1.03	
Razor chamber		0.55	−0.48	0.62	0.07	0.60	−1.02	
PinPoint 3D		0.86	−0.42	0.95	0.15	0.91	−1.10	
Semiflex 3D		1.64	−8.66	1.83	−0.04	1.78	−1.24	
Adv. Markus		1.88	−15.67	2.16	−0.35	2.10	−1.28	
	Passively scattered collimated - Aperture diameter [mm]							
	3		**5**		**10**		**15**		**20**
Detector	**$\Delta d_{80/20}$ [mm]**	**Diff. at (0,0) [%]**	**$\Delta d_{80/20}$ [mm]**	**Diff. at (0,0) [%]**	**$\Delta d_{80/20}$ [mm]**	**Diff. at (0,0) [%]**	**$\Delta d_{80/20}$ [mm]**	**Diff. at (0,0) [%]**	
microSilicon	0.10	−7.55	0.17	−0.47	0.17	−0.42	0.19	−0.13	
microDiamond	0.20	−15.79	0.35	−1.31	0.36	−0.26	0.38	−0.20	
Razor chamber	0.19	−15.41	0.33	−1.81	0.35	−0.50	0.37	−0.22	
PinPoint 3D	0.32	−25.36	0.54	−3.37	0.58	−0.24	0.59	−0.20	
Semiflex 3D	0.68	−52.95	1.06	−17.01	1.31	−0.45	1.31	−0.19	
Adv. Markus	0.77	−60.68	1.24	−24.34	1.59	−1.03	1.59	−0.23	

$\Delta d_{80/20}$ are associated with an uncertainty of 0.2 mm and the uncertainty for the difference at (0,0) was estimated to be 2%, 1%, 0.5%, and 0.2% for field sizes with side legths or diameters of 3, 5, 10 mm or larger, respectively.

3.3 | Collimated pencil beam scanning

Figure 3 shows the measured lateral dose profiles along the *x*-axis $D(x,y = 0)$ as determined from the film measurements of the *collimated PBS* fields with collimator diameters of 5, 10, and 15 mm. All fields show comparable $d_{80/20}$ between 0.7 and 0.8 mm, which are achieved by collimating PBS fields created without a range shifter. The corresponding computed signal profiles $M(x,y = 0)$ for various detectors from the convolution are presented alongside. The differences between $d_{80/20}$ values of the $M(x,y = 0)$ and that of the dose profiles as well as the signal reduction at the maximum are listed in Table 1. For all field sizes, the $M(x,y = 0)$ profiles show broader lateral penumbras than the $D(x,y = 0)$. This penumbra broadening is most pronounced for the Advanced Markus chamber ($\Delta d_{80/20}$ up to 2.2 mm) and least present in the $M(x,y = 0)$ of the microSilicon diode ($\Delta d_{80/20}$ up to 0.4 mm). For the smallest aperture diameter (5 mm), a reduction of the signal at the maximum of 8.7% (Semiflex 3D) and 15.7% (Advanced Markus) can also be observed.

3.4 | Passively scattered collimated proton fields

Figure 4 exemplarily shows the centered $M(x,y = 0)$ and $M(x = 0,y)$ of the *passively scattered* proton beam collimated by a 3 mm diameter aperture as measured with a microSilicon detector and a PinPoint 3D chamber along the *x*- and *y*-axis, respectively. In addition, the rotational

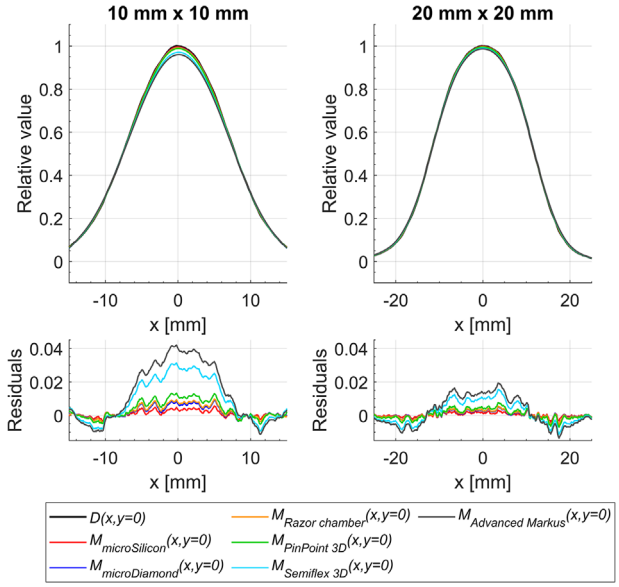

FIGURE 2 EBT3 film measured lateral dose profiles $D(x,y = 0)$ of square *PBS* fields with side lengths of 10 mm (left) and 20 mm (right) as well as the corresponding measured dose profiles $M(x,y = 0)$ obtained from the two-dimensional convolution of $D(x,y)$ and $K(x,y)$ for various point detectors. The relative values correspond to the profile values normalized to $D(x = 0,y = 0)$. The residuals represent the difference between the normalized $D(x,y = 0)$ and $M(x,y = 0)$ determined for each detector. [Color figure can be viewed at wileyonlinelibrary.com]

symmetrical profile $M_{sym}(x,y = 0)$, which was derived from averaging the four half profile sides is shown. The comparison between the individual points of the half profiles and $M_{sym}(x,y = 0)$ for which all profiles were normalized to the maximum of $M_{sym}(0,0)$ resulted in a maximum difference of 1.8% of the maximum.

Figure 5 shows the dose profiles $D_{PinPoint3D}(x,y = 0)$ and $D_{microSilicon}(x,y = 0)$ derived from the deconvolution in comparison to the measured $M_{Sym,PinPoint3D}(x,y = 0)$ and $M_{Sym,microSilicon}(x,y = 0)$ for the aperture diameters 3, 5, 10, and 15 mm. For ease of comparison, the profiles measured with the PinPoint 3D were multiplied by a cross-calibration factor determined as the ratio $\frac{M_{\text{microSilicon}}(x=0,y=0)}{M_{\text{PinPoint 3D}}(x=0,y=0)}$ from a 30 mm diameter field. The $d_{80/20}$ values of the derived $D_{PinPoint3D}(x,y = 0)$ and $D_{microSilicon}(x,y = 0)$ are given in Table 2 showing an agreement within 0.13 mm. Based on these results the uncertainty for calculating $\Delta d_{80/20}$ with the convolution model approach was estimated as 0.2 mm (Table 1).

When comparing the $M(x,y = 0)$ with the deconvolved $D(x,y = 0)$ profiles, the perturbation of the volume effect of the PinPoint 3D chamber can be identified for all four field sizes in terms of penumbra broadening. In addition, a reduction of the signal at the maximum of 23.5% and 3.7% can be seen for the PinPoint 3D chamber in the two smallest field sizes, 3 and 5 mm. The perturbation of the microSilicon diode, having a much smaller sensitive volume and narrower $K(x,y)$, is less pronounced and can only be seen in the 3 and 5 mm fields in terms of penumbra broadening and in the smallest field also in terms of a reduction of the signal at the maximum (7.0%).

TABLE 2 $d_{80/20}$ and difference in $d_{80/20}$ between $D_{PinPoint3D}(x,y = 0)$ and $D_{microSilicon}(x,y = 0)$ derived from the corresponding measured signal profiles $M_{Sym,PinPoint3D}(x,y = 0)$ and $M_{Sym,microSilicon}(x,y = 0)$ by iterative deconvolution with $K(x,y)$ of the PinPoint 3D and microSilicon in dependence of the aperture diameter of the *passively scattered collimated fields*.

	Aperture diameter [mm]			
	3	5	10	15
$d_{80/20}$ of $D_{microSilicon}(x,y = 0)$ [mm]	1.22	1.28	1.25	1.25
$d_{80/20}$ of $D_{PinPoint3D}(x,y = 0)$ [mm]	1.32	1.33	1.38	1.37
$\Delta d_{80/20}$ [mm]	−0.10	−0.05	−0.13	−0.12

To examine the influence of other detectors in the *passively scattered collimated* fields, detector signal profiles $M(x,y)$ were calculated from the convolution of $D_{microSilicon}(x,y)$ and the presented $K(x,y)$ of point detectors in Figure 1. Figure 6 shows the $M(x,y = 0)$ in comparison to $D_{microSilicon}(x,y = 0)$. Table 1 lists the increase in $d_{80/20}$ between the profiles as well as the percentage difference between the signal at position (0,0) with respect to $D_{microSilicon}(0,0)$.

Figure 6 and Table 1 show that measurements of the *passively scattered collimated* fields with the point detectors investigated in this work would all suffer from a broadening of the penumbra, which would be most pronounced for the Advanced Markus chamber ($\Delta d_{80/20}$ up to 1.6 mm) and least pronounced for the microSilicon diode ($\Delta d_{80/20}$ up to 0.2 mm). All $M(x,y = 0)$ of the 3 mm diameter field show a reduction of the signal at the maximum from 7.6% (microSilicon) to 60% (Advanced Markus). For the 5 mm diameter field the reduction of the signal at the maximum lies within the uncertainty for the microSilicon diode but can still be identified for all other detectors, varying between 1.3% (microDiamond) and 24.3% (Advanced Markus). In the 10 mm diameter field, a reduction of the signal at the maximum of 1% is only determined for the Advanced Markus chamber. No reduction was observed for all detectors in the 15 mm diameter field.

The left panel of Figure 7 shows the measured output ratios normalized to the 20 mm diameter field $\frac{M(x=0,y=0)}{M_{20\text{mm}}(x=0,y=0)}$ using the microSilicon, PinPoint 3D and microDiamond. The uncertainty for the output ratios considers the machine reproducibility of 1% (2σ) as specified by the manufacturer and the signal deviation resulted from a 0.2 mm positioning uncertainty based on the detailed analysis in Section 3.7. A value of 0.2 mm was chosen taking into account the PTW specification for the geometrical uncertainty of ±0.1 mm for the used

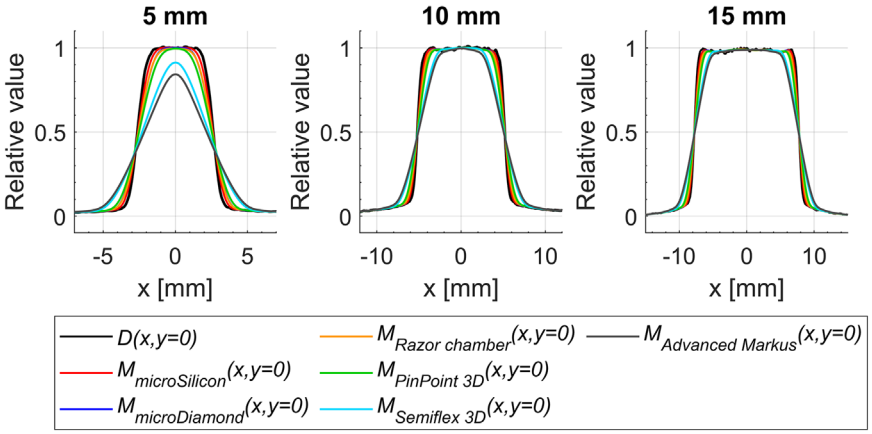

FIGURE 3 Lateral dose profiles $D(x,y = 0)$ of *collimated PBS* fields with circular collimators with opening diameters of 5 mm (left), 10 mm (middle), and 15 mm (right) as well as the corresponding signal profiles $M(x,y = 0)$ as obtained from the two-dimensional convolution of $D(x,y)$ and $K(x,y)$ for various point detectors. The relative values correspond to the profile values normalized to $D(x = 0,y = 0)$. [Color figure can be viewed at wileyonlinelibrary.com]

TABLE 3 Output correction factors k and corrected output factors determined for the detectors PinPoint 3D, microSilicon, and microDiamond for *passively scattered collimated* proton fields with aperture diameters from 3 to 30 mm.

Aperture diameter [mm]	Correction factor k			Corrected output factors		
	PinPoint 3D	microSilicon	microDiamond	PinPoint 3D	microSilicon	microDiamond
3	1.340(45)	1.082(37)	1.187(40)	0.901(37)	0.877(37)	0.884(37)
5	1.035(25)	1.005(24)	1.013(24)	0.973(29)	0.983(29)	0.967(28)
10	1.002(24)	1.004(24)	1.003(24)	0.989(29)	0.999(29)	0.993(29)
15	1.002(24)	1.001(24)	1.002(24)	1.004(30)	1.004(30)	1.002(30)
20	1.003(24)	1.005(24)	1.004(24)	1.003(30)	1.003(30)	1.004(30)
30	0.999(24)	0.999(24)	0.999(24)	0.995(29)	0.995(29)	0.994(29)

The value within parenthesis corresponds to the uncertainty in the last digit(s).

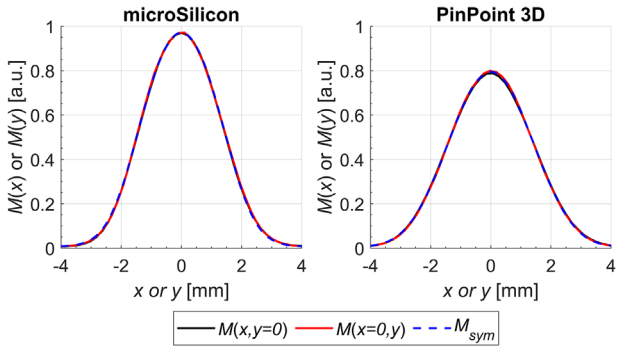

FIGURE 4 Centered signal profiles $M(x,y = 0)$ and $M(x = 0,y)$ of the 3 mm circular field measured with the microSilicon (left) and PinPoint 3D (right) as well as the corresponding rotational symmetrical profiles $M_{sym}(x,y = 0)$, which were determined by averaging the four half profiles. [Color figure can be viewed at wileyonlinelibrary.com]

phantom and the chosen step size (0.2 mm) of the profile measurements to center the detector.

The detector specific output correction factors k were derived from the ratio $\frac{D(x=0,y=0)/D_{20mm}(x=0,y=0)}{M(x=0,y=0)/M_{20mm}(x=0,y=0)}$ at the field center, where the dose profiles derived from the microSilicon measurements $D_{microSilicon}(x,y)$ were used in the numerator. Table 3 summarizes the resulting detector and field size specific output correction factors k by adopting the same consideration as above for the uncertainty estimation. The right panel of Figure 7 shows the corrected field output factors $\frac{D(x=0,y=0)}{D_{20mm}(x=0,y=0)}$ determined by multiplying $\frac{M(x=0,y=0)}{M_{20mm}(x=0,y=0)}$ with the corresponding k factor in Table 3. The sought average field output factors were calculated as the mean values of the three corrected detector measurements (diamonds in Figure 7, right panel). The percentage standard deviations of the average field output factors considering all three detectors were smaller than 0.5% for all field sizes except for the smallest 3 mm diameter field with a percentage standard deviation of 0.9%.

3.5 | Application of approximated $K_{area}(x,y)$

To estimate the impact of using an approximated convolution kernel based on the sensitive area of the detectors $K_{area}(x,y)$, Table 4 shows the difference in $d_{80/20}$ and in the signal reduction

at the maximum of the corresponding $M(x,y = 0)$ profiles and those obtained from using the $K(x,y)$ shown in Figure 1. Table 4 reveals differences in $d_{80/20}$ up to

TABLE 4 Difference in determined penumbra ($d_{80/20}$) and percentage point difference of the signal reduction at the field center (0,0) between measured signal profiles as predicted for point detectors by the convolution of $D(x,y)$ with the detectors lateral dose response function $K(x,y)$ or an approximated convolution kernel $K_{area}(x,y)$ exemplarily for the three smallest fields of investigated techniques, the 10 mm × 10 mm *PBS*, 5 mm *collimated PBS* and 3 mm *passively scattered collimated* field

	10 mm × 10 mm *PBS*		5 mm *collimated PBS*		3 mm *passively scattered collimated*	
	Difference in $d_{80/20}$ [mm]	Percentage point difference at (0,0)	Difference in $d_{80/20}$ [mm]	Percentage point difference at (0,0)	Difference in $d_{80/20}$ [mm]	Percentage point difference at (0,0)
microSilicon	0.00	0.04	0.00	0.04	0.00	−0.04
microDiamond	0.00	0.03	0.00	0.13	0.00	0.04
Razor chamber	0.01	0.24	0.05	0.76	0.02	2.27
PinPoint 3D	0.00	0.03	−0.04	0.39	−0.02	−0.65
Semiflex 3D	−0.01	−0.09	−0.13	0.44	0.00	−2.99
Adv. Markus	0.03	0.74	0.04	5.22	0.07	2.02

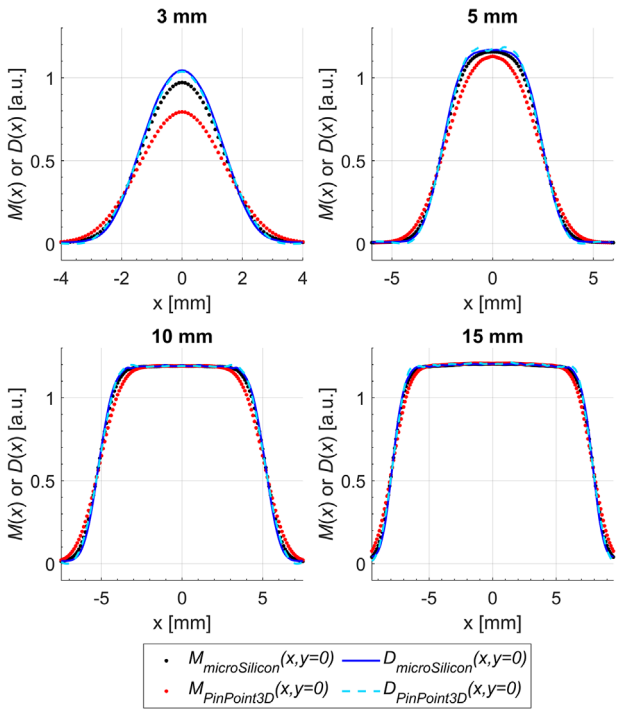

FIGURE 5 Dose profiles $D_{PinPoint3D}(x,y = 0)$ and $D_{microSilicon}(x,y = 0)$ from deconvolution in comparison to the corresponding $M_{PinPoint3D}(x,y = 0)$ and $M_{microSilicon}(x,y = 0)$ for the four smallest field sizes (3 mm, 5 mm, 10 and 15 mm) investigated for the *passively scattered collimated* proton beam delivery technique. The $M_{PinPoint3D}(x,y = 0)$ profiles were scaled by a cross-calibration factor to be comparable to the $M_{microSilicon}(x,y = 0)$ (compare text). The corresponding $D(x,y = 0)$ were obtained from deconvolving the presented $M(x,y = 0)$. [Color figure can be viewed at wileyonlinelibrary.com]

0.13 mm (Semiflex 3D in the 5 mm *collimated PBS* field). The percentage point difference of the signal reduction at the maximum is less than 1% for the diode type detectors and most chamber-field size combinations, but becomes larger for ionization chambers with greater signal reductions at the maximum.

3.6 | Signal theoretical analysis

The left panel in Figure 8 shows the Fourier transform of the dose profiles with the smallest lateral width FT[$D(x,y = 0)$] for each delivery technique investigated in this work (10 mm × 10 mm *PBS* field, 5 mm diameter *collimated PBS* field, 3 mm diameter *passively scattered collimated* field). The 3 mm diameter *passively scattered collimated* field exhibits the highest frequency components followed by the 5 mm diameter *collimated PBS* field and the 10 mm × 10 mm *PBS* field.

The Fourier transforms of the lateral dose response functions of microSilicon, PinPoint 3D, Semiflex 3D and Advanced Markus FT[$K(x,y = 0)$] are shown in the right panel of Figure 8. All lateral response functions presented in the right panel of Figure 8 serve as low-pass filter during the measurement process attenuating high-frequency components present in the dose profiles according to Equation 5. The cutoff frequency of these functions defined at FT[$K(x,y = 0)$] = 0.5[43] corresponds to 0.41, 0.22, 0.13, and 0.12 mm^{-1} for the microSilicon, PinPoint 3D, Semiflex 3D, and Advanced Markus, respectively. In other words, the smaller the dimensions of the detector, the higher is the cutoff frequency.

Considering their low-pass filter property, the suitability of the detector can be evaluated by comparing the maximum frequency components present in the dose profiles and the cutoff frequency associated with the detectors. For example, the maximum frequency component of the 10 mm × 10 mm *PBS* field is approximately 0.1 mm^{-1} which is less than the cutoff frequencies of all the detectors including the Advanced Markus chamber. As a consequence, measurements of the 10 mm × 10 mm *PBS* profile are not largely perturbed by these detectors resulting in the good agreement between $M(x,y = 0)$ and $D(x,y = 0)$ as presented in Figure 2. In contrast, the maximum frequencies of the 5 mm diameter *collimated PBS* field and 3 mm diameter *passively scattered collimated* field exceed

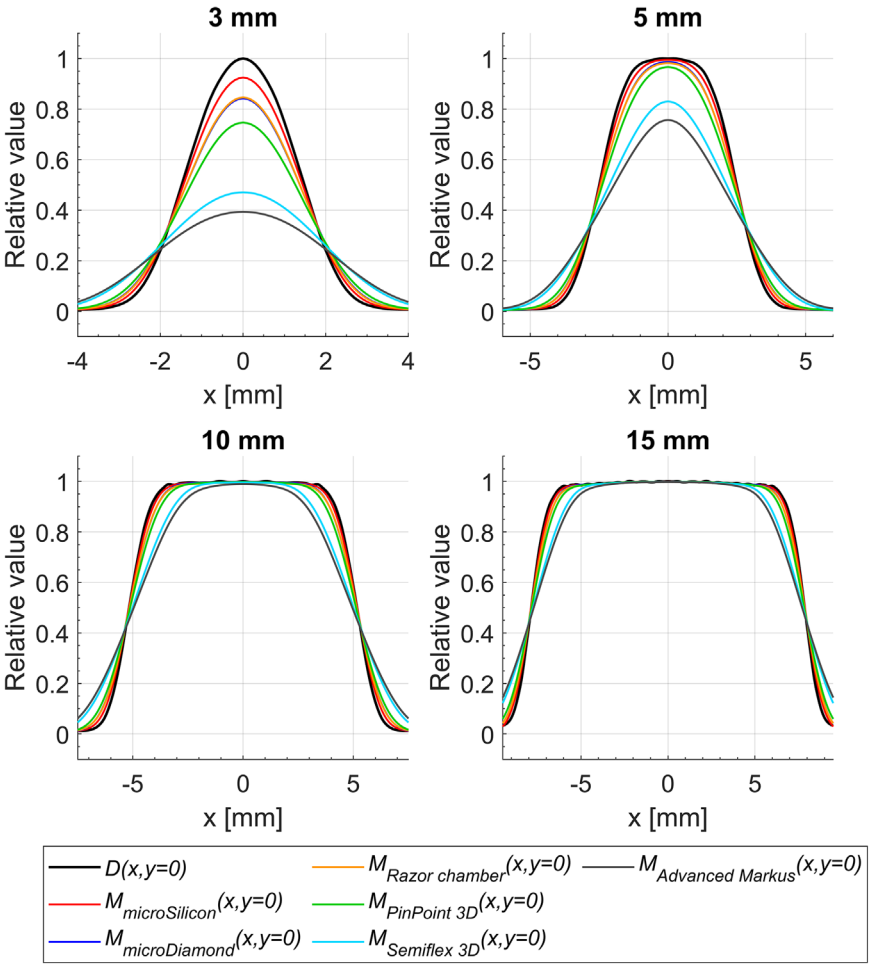

FIGURE 6 Lateral dose profiles $D_{microSilicon}(x,y)$ of *passively scattered collimated* fields using circular apertures with opening diameters of 3 mm (upper left), 5 mm (upper right), 10 mm (lower left) and 15 mm (lower right) as well as the corresponding measured dose profiles obtained from the convolution of $D_{microSilicon}(x,y)$ and $K(x,y)$ of the corresponding detectors. The relative values correspond to the profile values normalized to $D(x = 0,y = 0)$. [Color figure can be viewed at wileyonlinelibrary.com]

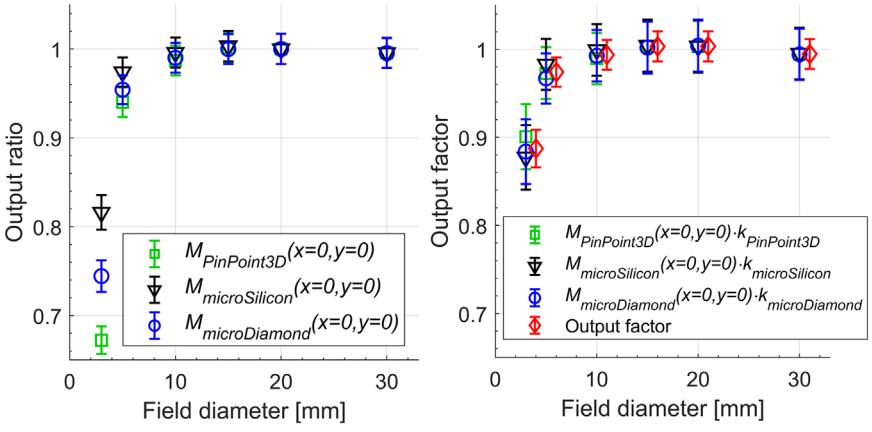

FIGURE 7 Output ratios $\frac{M(x=0,y=0)}{M_{20mm}(x=0,y=0)}$ (left) measured with the PinPoint 3D, microSilicon, and microDiamond in *passively scattered collimated* proton fields and corrected output factors determined after application of the correction factors k (see Table 3) $\frac{D(x=0,y=0)}{D_{20mm}(x=0,y=0)}$ from which an average output factor (red diamonds given a shift of 1 mm for better visibility) was calculated (right). The errorbar for the average output factor (red diamonds) corresponds to the standard error of the mean. [Color figure can be viewed at wileyonlinelibrary.com]

the cutoff frequencies of the PinPoint 3D, Semiflex 3D and Advanced Markus that would result in the strong perturbation demonstrated in Figures 3 and 6.

3.7 | Influence of detector positioning errors

Figure 9 shows the percentage signal reductions in the $M(x,y = 0)$ at different off-axis x-positions that could be resulted from positioning error. Note that, the values $(1 - \frac{M(x,y=0)}{M(x=0,y=0)}) \cdot 100$ presented in Figure 9 correspond to the signal reduction due to positioning errors only and the perturbation due to the volume effect, that is, the difference between $M(x = 0,y = 0)$ and $D(x = 0,y = 0)$, must be additionally considered to estimate the overall error. Figure 9 shows that the smallest fields are influenced the strongest by positioning errors. For the smallest 3 mm *passively scattered collimated* field, the largest

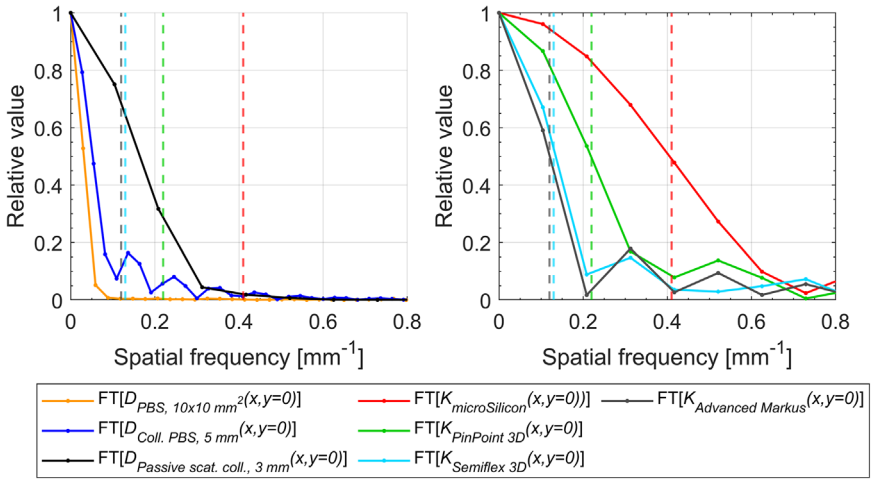

FIGURE 8 Left: FT[$D(x,y=0)$] of dose profiles of the smallest proton fields investigated in this work (10 mm × 10 mm *PBS* field, 5 mm diameter *collimated PBS* field, 3 mm diameter *passively scattered collimated* field). Right: FT[$K(x,y=0)$] of the $K(x,y=0)$ of selected point detectors (microSilicon, PinPoint 3D, Semiflex 3D and Advanced Markus). The vertical dashed lines indicate the cutoff frequencies at FT[$K(x,y=0)$] = 0.5 of the point detectors. All profiles are maximum normalized. [Color figure can be viewed at wileyonlinelibrary.com]

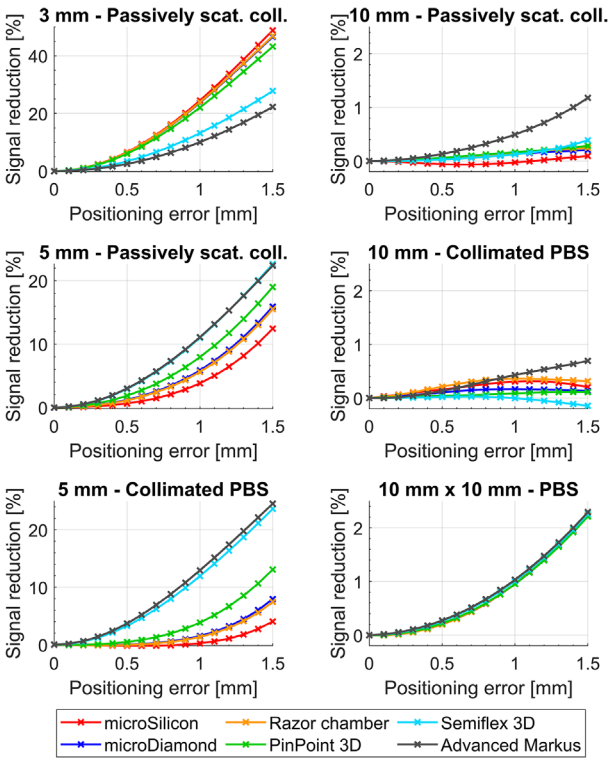

FIGURE 9 Percentage signal reduction in the $M(x,y=0)$ with respect to the corresponding $M(0,0)$ in dependence of a positioning error for selected fields from the three delivery techniques. [Color figure can be viewed at wileyonlinelibrary.com]

signal reduction due to a 0.5 mm positioning error can be observed for the microSilicon that amounts to 6.6%. In contrast, the impact of positioning errors in larger collimated fields, such as a 5 mm diameter field, becomes less prominent for small detectors. Of all 10 mm fields (right column in Figure 9) the 10 mm × 10 mm *PBS* field is most sensitive to detector positioning errors but shows a similar signal reduction in dependence of the off-axis position for all detectors. The 10 mm diameter collimated fields are more robust to positioning errors with positioning errors up to 1.5 mm leading to signal reductions withtin 0.5% for all detectors, except for the Advanced Markus chamber for which the signal reduction is up to 1.2%.

4 | DISCUSSION

4.1 | Detector choice based on delivery techniques

The comparison between the dose distributions of small clinical proton fields delivered using three different techniques and the corresponding detector measurements presented in this work have clearly demonstrated the challenges associated with the correct dosimetric characterization of these fields. More importantly, the results reveal that the suitability of point detectors depends on the delivery technique, field size, beam collimation and detector's lateral dose response function. Based on these results, the clinical recommendations presented in the following sections can be derived. It should be mentioned that the fields investigated in this work serve as examples for the considered techniques. Nonetheless, other parameters like incident energies or measurement depths can lead to different lateral penumbras or field shape. Consequently, individual measurement conditions require separate considerations to conclude on the suitability of the detector's choice.

4.1.1 | Pencil beam scanning fields

The $d_{80/20}$ of the 10 mm × 10 mm and 20 mm × 20 mm *PBS* proton fields studied in this work were 6.9 mm and 8.7 mm, respectively. The achievable steepness of PBS fields, including the small fields investigated in this study, is limited by that of the single pencil beams so that the lateral penumbra widths of *PBS* fields are generally larger than those of an individual pencil beam.

As shown in Figure 8, the frequency analysis of the smallest *PBS* field (10 mm × 10 mm) showed

frequency components below approximately 0.1 mm^{-1}, which is in accordance with a previously performed frequency analysis of intensity modulated proton therapy treatment plans.[13] Since the cutoff frequencies of all investigated detectors are larger than the frequencies associated with *PBS*, the Gaussian shaped *PBS* fields are not expected to suffer from detector's volume effect perturbations. Therefore, the predicted $M(x,y)$ derived by convolution of film measured $D(x,y)$ with $K(x,y)$ only showed differences in $d_{80/20}$ smaller than 0.25 mm for all investigated detectors and both field sizes.

For some detectors in PBS fields, similar findings were presented in the past.[13,15,17,29,45,46] Schwaab et al.,[16] Sahoo et al.[15] and Sawakuchi et al.[45] measured proton and/or carbon ion pencil beam profiles with ionization chambers and concluded that the effect of detector size can be neglected for the Gussian like lateral profiles in scanned fields.[15,16,29,45] Furukawa et al. and Brodbek et al.[13] showed that the volume effect of ionization chambers of 2D arrays only has a minor or even negligible impact on the plan verification process of the intensity modulated carbon ion or proton therapy fields studied.[13,17] Moignier et al.[46] simulated profiles of a 100 MeV proton pencil beam with a full width at half maximum (FWHM) of 5 mm using sensitive diamond crystal volumes of widths between 0.25 and 4 mm. Their results also showed no volume averaging effect for detector widths of 1 mm or less. However, they found an increased measured lateral penumbra for detectors with larger active surface at this small field size.[46] Grevillot et al.[47] investigated several detectors and phantoms for commissioning a light ion beam facility. A comparison of lateral profiles measured with a PinPoint chamber and microDiamond detector revealed a constant underestimation of the fields FWHM measured with the microDiamond, which Grevillot et al. attribute to the PinPoints larger cavity diameter.[47] In the Task group 224 report on proton therapy machine QA,[8] small point-like ionization chambers are listed as suitable detectors for measuring scanned beam profiles, which can be confirmed by the results presented in our work. According to a review of clinical dosimetry in scanned ion beam dosimetry, PinPoint type ionization chambers with radii smaller 1.5 mm should be used for point dose measurements in gradient regions,[48] which is supported by the negligible increase in $d_{80/20}$ of *PBS* fields found in this work. For lateral dose profile acquisition, Giordanengo, Manganaro and Vignati[48] list films, scintillation screens and diodes as detectors for commissioning in scanned ion beams and add ministrips ionization chambers as suitable detector for quality assurance measurements.[48]

In this work, the signal reduction at the maximum in the smallest *PBS* field (10 mm × 10 mm) was estimated to be 2.9% and 4% for the two largest detectors used, Semiflex 3D and Advanced Markus, and between 1.2% and 0.8% for smaller ionization chambers like the Razor chamber and PinPoint 3D, respectively. Harms et al. measured output in 70 MeV PBS fields with a CC04 ionization chamber, films and a scintillation screen and determined differences of the chamber's signal of 3.6% and 0.8% in the smallest field size of 20 mm width from the film and scintillator measurements, respectively.[49] Recently, Kugel et al. estimated the standard uncertainty from disregarding volume averaging in dependence of the PBS field size and incident proton energy for a CC01 ionization chamber (IBA Dosimetry, Schwarzenbruck, Germany) having the same inner diameter as the Razor chamber.[4] In that work the uncertainty of measuring a small 160 MeV 10 mm × 10 mm proton field with the CC01 was determined to be approximately 0.9%.[4] Following the same methodology as described in the paper, the authors also investigated other detectors and provided the corresponding uncertainties for the microSilicon detector and PinPoint 3D chamber of 0.2% and 1%, respectively, in private communication. Their results are in good agreement with the reduction of the signal at the maximum calculated in this work for the investigated dectectors (0.8% for Razor chamber, 0.3% for microSilicon and 1.2% for PinPoint 3D).

4.1.2 | Proton fields combined with collimators

In comparison to PBS fields, lateral penumbras of collimated proton fields are greatly reduced. The $d_{80/20}$ values of the dose profiles are 0.8 mm for all three *collimated PBS* fields with diameters between 5 and 15 mm, while the $d_{80/20}$ of the *passively scattered collimated* fields for which no range shifter was used are around 1.3 mm for all aperture diameters between 3 and 20 mm (Table 2). Due to the use of apertures in combination with the thereby smaller field sizes achievable, the frequency components of these collimated fields are higher than in PBS fields as shown in Figure 8, where the frequency components in the 5 mm diameter *collimated PBS* field and the 3 mm diameter *passively scattered collimated* field exceed the cutoff frequencies of the ionization chambers. This implies that measurements with such chambers in collimated proton fields will be perturbed, which can also be seen in Figures 3 and 6.

For the *collimated PBS* fields, the computed $\Delta d_{80/20}$ values reveal a broadening of the measured lateral penumbra by all investigated detectors. As the $d_{80/20}$ of the dose profiles for these fields are approximately the same (between 0.7 and 0.8 mm), the magnitudes of penumbra broadening, $\Delta d_{80/20}$, caused by each detector are also comparable among the field sizes between 5 and 15 mm with values up to 0.35 mm for the microSilicon, 0.65 mm for the microDiamond, 0.62 mm for the Razor chamber, 0.95 mm for the PinPoint 3D, 1.84 mm for the Semiflex 3D, and 2.16 mm for the Advanced Markus.

The same can also be observed for the passively scattered collimated fields, whereas the penumbra broadening, $\Delta d_{80/20}$, are slightly smaller than that experienced in *collimated PBS* fields. This can be partly attributed to the larger $d_{80/20}$ of the dose profiles (1.3 mm) as lower proton energies and more scatterers are used in these ocular treatment fields.

Several studies have also investigated potential perturbations from detectors in lateral profile measurements of collimated proton fields. For example, McAuley et al.[50] found only small difference between the collimated scattered profiles measured with high resolution film and a diode detector operated in radial orientation having an especially small cross-sectional width of 20 μm.[50] Marsolat et al.[1] investigated microDiamond detectors in a passively scattered collimated proton beam with an energy of 138 MeV and found increased penumbras by approximately 0.3 mm in comparison to penumbra measured with an SFD diode. In addition, they operated the detectors oriented perpendicular to the beam by which they were able to obtain even lower penumbras than those measured with the SFD diode indicating a much better resolution due to the small thickness of the diamond in that orientation (1 μm).[1] Recently, spectral fiber dosimetry using beryllium oxide as radioluminescent material with high spatial resolution has been applied to acquire proton beam profiles and depth dose distributions.[51]

In addition to films and scintillation screens, Task group 224 report[8] lists small point-like ionization chambers as suitable for scanned and scattered beam profile measurements. Although the maximum penumbra increase identified with such small ionization chambers in this work of 0.62 mm (Razor chamber) and 0.94 mm (PinPoint 3D) is within the tolerances for $d_{80/20}$ suggested in the Task group 224 report of $\pm$ 2 mm, this penumbra increase is still quite large with respect to the small field sizes investigated in this work. As a consequence, the recommendations may need to be adapted to lateral profile measurements of such small fields. As shown in this study, higher accuracy can be achieved in these cases either by using detectors like the microSilicon diode or by correcting the measurements acquired using ionization chambers as demonstrated in this work. For passive scattering proton beam dosimetry under non-reference conditions, Rath and Sahoo mention several detectors as suitable for lateral profile measurements including small-volume ionization chambers and point out that such measurements may need a correction for the detector size effect,[29] which is supported by our results.

A strong reduction of the signal at the maximum was found for the small collimated fields studied in this work. When measuring the 5 mm *collimated PBS* field using the two detectors with the largest sensitive area, a reduction of the signal at the maximum of 8.7% and 15.7% was determined for the Semiflex 3D and Advanced Markus, respectively. In the 3 mm diameter *passively scattered collimated* field this reduction was even larger of up to 52.9% (Semiflex 3D) and 60.7% (Advanced Markus).

Perturbations in output factor measurements of collimated fields have already been described in the past. Andersen et al.[2] measured dose output in proton beams collimated with apertures between 5 and 100 mm using radiochromic film and a microDiamond detector, and found differences between both detectors of up to 70%.[2] Hoehr et al.[12] identified differences in output factor measurements for collimated 74 MeV scattered proton fields down to 5 mm diameter. Their investigation included a scintillation detector, a diamond detector oriented perpendicular to the beam direction and a silicon diode detector, of which the latter had the largest cross-sectional area of 2.65 mm $\times$ 2.65 mm and showed a relative signal difference of 2% for the smallest field size, which the authors attributed to larger volume averaging.[12] Fleury et al.[20] measured output ratios for *passively scattered collimated* fields dedicated for eye treatments with an Advanced Markus chamber having a comparably large sensitive area but found no remarkable change in the Dose/MU ratios in dependence of the field size for field sizes between 10 and 35 mm diameter.[20] This is in agreement with our prediction for the measurement with the Advanced Markus chamber of 10 mm diameter fields for which we estimated the signal reduction caused by the Advanced Markus chamber to be only 0.4% (*collimated PBS*) and 1% (*passively scattered collimated*). Fleury et al. emphasized that for fields smaller than 10 mm diameter, proper considerations of small field dosimetry should be made. This statement is supported by our investigation of fields with smaller diameter for which the volume effect of the Advanced Markus chamber leads to a noteworthy reduction of the signal at the maximum of up to 60.7% (3 mm diameter *passively scattered collimated* field) indicating that a higher resolution detector would be necessary to accurately measure the dose in these smaller field sizes.[20] Vatnitsky et al.[10] investigated dosimetry techniques for stereotactic proton fields and measured output factors for two scattered proton beams of 127 MeV or 155 MeV collimated with collimators between 2 and 30 mm diameter. Vatnitsky et al. considered a large set of detectors and concluded that the investigated point detectors may only be used for measurements in collimated fields with diameters greater than 8 mm. While they list a diode and a TLD detector to be suitable for characterizing the 8 mm field, they stated that a PinPoint ionization chamber and diamond detector should only be used for collimators of 10 mm diameter or larger, and even larger detectors (Extradin T1 and PTW Markus chamber) are only considered accurate for collimators of 20 mm diameter or larger.[10]

4.2 | Correction strategies with lateral dose response functions

In this work, rotational symmetrical $K(r)$ were determined from experimentally derived or Monte Carlo simulated $K(x)$ for six detectors in proton fields that can be used to correct the perturbations of point detectors in lateral dose profile or output factor measurements. This has been demonstrated for measurements of *passively scattered collimated* proton fields, where the undisturbed $D(x,y)$ have been derived from the deconvolution of $M(x,y)$ measured using a microSilicon detector and PinPoint 3D chamber with the respective $K(x,y)$. The comparison of the resulting dose profiles $D_{PinPoint3D}(x,y=0)$ and $D_{microSilicon}(x,y=0)$ showed an overall good agreement with maximum differences in the $d_{80/20}$ of 0.13 mm (Table 2).

Output measurements in *passively scattered collimated* proton fields were performed with a microSilicon, microDiamond and PinPoint 3D and corrected with output correction factors k in Table 3. After the corrections, the percentage standard deviation of the average field output factors considering all three detectors was within 1% indicating the suitability of the proposed correction strategy based on the detector $K(x,y)$. It is noteworthy that the magnitude of k depends strongly on the shape of the underlying dose profiles and the correction factors in Table 3 should be validated before they can be applied for other small proton fields. Despite the good consistency of the corrected output factors as presented in the right panel of Figure 7, one should avoid using detectors that require large corrections[6] such as the PinPoint 3D chamber or microDiamond with $k = 1.340$ and 1.187 for the 3 mm field size, respectively. The most suitable detector in this case is in fact the microSilicon with the smallest sensitive area. Nevertheless, the numerical values in Table 3 could still be helpful to guide the detector choice and estimate the measurement uncertainty.

The investigation of using an approximated convolution kernel based on the detectors sensitive areas (compare Table 4) shows differences in $d_{80/20}$, as predicted from using the two convolution kernels, $K(x,y)$ and $K_{area}(x,y)$, up to 0.13 mm and percentage point differences of the signal reduction at the maximum below 1% for the diode type detectors and most chamber-field size combinations, but becomes larger for ionization chambers. For example, the signal reduction from using the Advanced Markus chamber in the 5 mm collimated PBS field is estimated to be 16% using $K(x,y)$ and 11% using $K_{area}(x,y)$. Similar differences can be observed in the 3 mm *passively scattered collimated* field, where the ionization chambers Razor chamber, Semiflex 3D and Advanced Markus also show some higher percentage point differences up to 3%. The larger difference observed for the ionization chambers can be partly attributed to the negligence of the density perturbation caused by the low density air volume when using $K_{area}(r)$. Furthermore, the approximation of the sensitive volume by considering solely the detector radius may cause additional discrepancy as the geometry of their sensitive volume is more complex due to the spherical chamber tip and the presence of nonsensitive air volume adjacent to the chamber's stem.[52]

4.3 | Detector positioning

To estimate the role of an accurate positioning of the detectors in the fields center during output measurements in small fields, positioning errors were simulated for selected $M(x,y)$. The results in Figure 9 show that the smallest fields are influenced the strongest by errors in positioning. For the smallest 3 mm *passively scattered collimated* field, the signal reduction due to a 0.5 mm positioning error was found for the microSilicon of up to 6.6%. Considering that the microSilicon is the detector with the smallest sensitive volume this observation may be surprising at first but this is a result of the steep $M(x,y=0)$ profile (compare Figure 6) measured with the microSilicon that resembles closest the $D(x,y=0)$ making it much more sensitive to changes in position. For the larger chambers, such as the Advanced Markus chamber, the steepness of the measured $M(x,y=0)$ has been strongly reduced by the volume effect so that it is less sensitive to detector positioning errors.

In contrast, the impact of positioning errors in larger collimated fields becomes less prominent for small detectors as the profiles feature a plateau region that is least affected by the volume effect associated with small detectors. However, as demonstrated previously in Figures 3 and 6, this plateau region vanishes when measured with large detectors, so that $M(x,y=0)$ profiles become steeper around the maximum and therefore more susceptible to positioning errors.

The comparison of the results of the 10 mm × 10 mm *PBS* field and 10 mm diamater collimated fields (right panels in Figure 9) shows that, on the one hand, the *PBS* field is more sensitive to positioning errors due to the non-vanishing dose gradient around its maximum. On the other hand, the collimated fields associated with a relatively homogenous plateau are more robust to positioning errors such that the percentage signal reduction associated with positioning errors up to 1.5 mm of all detectors, except for the Advanced Markus chamber, is within 0.5%.

5 | CONCLUSION

Point detector measurements in small fields can be challenging because the extended detector volume can perturb the measurements leading to inadequate representation of the actual dose distributions. To address this issue, we investigated the suitability and accuracy

of six clinical point detectors for lateral dose profile and output measurements in small proton fields. Generic correction strategies based on a convolution model in combination with detector specific lateral dose response functions $K(x,y)$ were used to estimate or to correct for perturbations in these fields created via *PBS*, *collimated PBS* and a *passively scattered collimated* proton therapy delivery techniques. While the difference between $D(x,y)$ and $M(x,y)$ of *PBS* fields was generally small, stronger detector perturbations were identified in collimated proton fields associated with a steep lateral penumbra. The findings of this work can guide the detector selection for lateral dose profile and output factor measurements in small proton fields with regard to the different delivery techniques. The results can contribute to the development of a code of practice for small field proton dosimetry in the future.

ACKNOWLEDGMENTS

The authors would like to thank Sytze Brandenburg and Emiel van der Graaf for fruitful discussions on the presented results. Monte Carlo simulations were performed on the HPC Cluster CARL funded by the DFG under INST 184/157-1 FUGG.

Open access funding enabled and organized by Projekt DEAL.

CONFLICT OF INTEREST

The authors have no relevant conflicts of interest to disclose.

REFERENCES

1. Marsolat F, De Marzi L, Patriarca A, et al. Dosimetric characteristics of four PTW microDiamond detectors in high-energy proton beams. *Phys Med Biol*. 2016;61(17):6413-6429. doi:10.1088/0031-9155/61/17/6413
2. Andersen A, Coutinho L, Das I. SU-D-304-03: small field proton dosimetry using MicroDiamond and Gafchromic film. *Med Phys*. 2015;42(6):3208-3208. doi:10.1118/1.4923862
3. Lomax A. What will the medical physics of proton therapy look like 10 yr from now? A personal view. *Med Phys*. 2018;45(11):e984-e993. doi:10.1002/mp.13206
4. Kugel F, Wulff J, Bäumer C, et al. Validating a double Gaussian source model for small proton fields in a commercial Monte-Carlo dose calculation engine. *Z Für Med Phys*. Published online December 2022:S0939388922001325. doi:10.1016/j.zemedi.2022.11.011
5. Das IJ, Francescon P, Moran JM, et al. Report of AAPM Task Group 155: megavoltage photon beam dosimetry in small fields and non-equilibrium conditions. *Med Phys*. 2021;48(10). doi:10.1002/mp.15030
6. Palmans H, Andreo P, Huq MS, Seuntjens J. *Dosimetry of Small Static Fields Used in External Beam Radiotherapy: An International Code of Practice for Reference and Relative Dose Determination*. International Atomic Energy Agency; 2017.
7. Sahoo N, Zhu XR, Arjomandy B, et al. A procedure for calculation of monitor units for passively scattered proton radiotherapy beams: mU calculation for passively scattered proton therapy beams. *Med Phys*. 2008;35(11):5088-5097. doi:10.1118/1.2992055
8. Arjomandy B, Taylor P, Ainsley C, et al. AAPM task group 224: comprehensive proton therapy machine quality assurance. *Med Phys*. 2019;46(8):e678-e705. doi:10.1002/mp.13622
9. Grevillot L, Osorio Moreno J, Letellier V, et al. Clinical implementation and commissioning of the MedAustron Particle Therapy Accelerator for non-isocentric scanned proton beam treatments. *Med Phys*. 2020;47(2):380-392. doi:10.1002/mp.13928
10. Vatnitsky SM, Miller DW, Moyers MF, et al. Dosimetry techniques for narrow proton beam radiosurgery. *Phys Med Biol*. 1999;44(11):2789-2801. doi:10.1088/0031-9155/44/11/308
11. Karger CP, Jäkel O, Palmans H, Kanai T. Dosimetry for ion beam radiotherapy. *Phys Med Biol*. 2010;55(21):R193-R234. doi:10.1088/0031-9155/55/21/R01
12. Hoehr C, Lindsay C, Beaudry J, et al. Characterization of the exradin W1 plastic scintillation detector for small field applications in proton therapy. *Phys Med Biol*. 2018;63(9):095016. doi:10.1088/1361-6560/aabd2d
13. Brodbek L, Kretschmer J, Willborn K, et al. Analysis of the applicability of two-dimensional detector arrays in terms of sampling rate and detector size to verify scanned intensity-modulated proton therapy plans. *Med Phys*. 2020;47(9):4589-4601. doi:10.1002/mp.14346
14. Kretschmer J, Brodbek L, Looe HK, et al. Investigating the lateral dose response functions of point detectors in proton beams. *Phys Med Biol*. 2022;67(14):145003. doi:10.1088/1361-6560/ac783c
15. Sahoo N, Ciangaru G, Sawakuchi G, et al. SU-GG-T-463: study of the magnitude of detector size effect in the measured lateral profiles of proton pencil beam spots. *Med Phys*. 2010;37(6Part23):3293-3293. doi:10.1118/1.3468861
16. Schwaab J, Brons S, Fieres J, Parodi K. Experimental characterization of lateral profiles of scanned proton and carbon ion pencil beams for improved beam models in ion therapy treatment planning. *Phys Med Biol*. 2011;56(24):7813-7827. doi:10.1088/0031-9155/56/24/009
17. Furukawa T, Inaniwa T, Hara Y, Mizushima K, Shirai T, Noda K. Patient-specific QA and delivery verification of scanned ion beam at NIRS-HIMAC: qA and verification for scanning delivery. *Med Phys*. 2013;40(12):121707. doi:10.1118/1.4828845
18. Peucelle C, Nauraye C, Patriarca A, et al. Proton minibeam radiation therapy: experimental dosimetry evaluation: proton minibeam radiation therapy: experimental evaluation. *Med Phys*. 2015;42(12):7108-7113. doi:10.1118/1.4935868
19. Vernimmen F. Intracranial stereotactic radiation therapy with charged particle beams: an opportunity to regain the momentum. *Int J Radiat Oncol*. 2016;95(1):52-55. doi:10.1016/j.ijrobp.2015.10.016
20. Fleury E, Trnková P, Spruijt K, et al. Characterization of the HollandPTC proton therapy beamline dedicated to uveal melanoma treatment and an interinstitutional comparison. *Med Phys*. 2021;48(8):4506-4522. doi:10.1002/mp.15024
21. Safai S, Bortfeld T, Engelsman M. Comparison between the lateral penumbra of a collimated double-scattered beam and uncollimated scanning beam in proton radiotherapy. *Phys Med Biol*. 2008;53(6):1729-1750. doi:10.1088/0031-9155/53/6/016
22. Winterhalter C, Lomax A, Oxley D, Weber DC, Safai S. A study of lateral fall-off (penumbra) optimisation for pencil beam scanning (PBS) proton therapy. *Phys Med Biol*. 2018;63(2):025022. doi:10.1088/1361-6560/aaa2ad
23. Wulff J, Koska B, Janson M, et al. Technical note: impact of beam properties for uveal melanoma proton therapy—An in silico planning study. *Med Phys*. 2022;49(5):3481-3488. doi:10.1002/mp.15573.
24. Hyer DE, Hill PM, Wang D, Smith BR, Flynn RT. A dynamic collimation system for penumbra reduction in spot-scanning proton therapy: proof of concept: penumbra trimmer for spot scanning. *Med Phys*. 2014;41(9):091701. doi:10.1118/1.4837155
25. Bäumer C, Fuentes C, Janson M, Matic A, Timmermann B, Wulff J. Stereotactical fields applied in proton spot scanning

mode with range shifter and collimating aperture. *Phys Med Biol*. 2019;64(15):155003. doi:10.1088/1361-6560/ab2ae7
26. Bäumer C, Plaude S, Khalil DA, et al. Clinical implementation of proton therapy using Pencil-Beam scanning delivery combined with static apertures. *Front Oncol*. 2021;11:599018. doi:10.3389/fonc.2021.599018
27. Ciocca M, Magro G, Mastella E, et al. Design and commissioning of the non-dedicated scanning proton beamline for ocular treatment at the synchrotron-based CNAO facility. *Med Phys*. 2019;46(4):1852-1862. doi:10.1002/mp.13389
28. Grewal HS, Ahmad S, Jin H. Characterization of penumbra sharpening and scattering by adaptive aperture for a compact pencil beam scanning proton therapy system. *Med Phys*. 2021;48(4):1508-1519. doi:10.1002/mp.14771
29. Rath AK, Sahoo N. *Particle Radiotherapy*. 2016. doi:10.1007/978-81-322-2622-2
30. Looe HK, Stelljes TS, Foschepoth S, Harder D, Willborn K, Poppe B. The dose response functions of ionization chambers in photon dosimetry – Gaussian or non-Gaussian? *Z Für Med Phys*. 2013;23(2):129-143. doi:10.1016/j.zemedi.2012.12.010
31. Harder D, Looe HK, Poppe B. Convolutions and deconvolutions in radiation dosimetry. *Comprehensive Biomedical Physics*. Elsevier; 2014:249-269. doi:10.1016/B978-0-444-53632-7.00913-8
32. Poppinga D, Meyners J, Delfs B, et al. Experimental determination of the lateral dose response functions of detectors to be applied in the measurement of narrow photon-beam dose profiles. *Phys Med Biol*. 2015;60(24):9421-9436. doi:10.1088/0031-9155/60/24/9421
33. Looe HK, Harder D, Poppe B. Understanding the lateral dose response functions of high-resolution photon detectors by reverse Monte Carlo and deconvolution analysis. *Phys Med Biol*. 2015;60(16):6585-6607. doi:10.1088/0031-9155/60/16/6585
34. Laub WU, Wong T. The volume effect of detectors in the dosimetry of small fields used in IMRT. *Med Phys*. 2003;30(3):341-347. doi:10.1118/1.1544678
35. Poppinga D, Delfs B, Meyners J, Harder D, Poppe B, Looe HK. The output factor correction as function of the photon beam field size – direct measurement and calculation from the lateral dose response functions of gas-filled and solid detectors. *Z Für Med Phys*. 2018;28(3):224-235. doi:10.1016/j.zemedi.2017.07.006
36. MATLAB. *Version 9.7.0.1190202 (R2019b)*. The MathWorks Inc. 2019.
37. Slopsema RL, Mamalui M, Zhao T, Yeung D, Malyapa R, Li Z. Dosimetric properties of a proton beamline dedicated to the treatment of ocular disease: dosimetry of a proton eyeline. *Med Phys*. 2013;41(1):011707. doi:10.1118/1.4842455
38. Agostinelli S, Allison J, Amako K, et al. Geant4—a simulation toolkit. *Nucl Instrum Methods Phys Res Sect Accel Spectrometers Detect Assoc Equip*. 2003;506(3):250-303. doi:10.1016/S0168-9002(03)01368-8
39. Jan S, Benoit D, Becheva E, et al. GATE V6: a major enhancement of the GATE simulation platform enabling modelling of CT and radiotherapy. *Phys Med Biol*. 2011;56(4):881-901. doi:10.1088/0031-9155/56/4/001
40. Marchand EW. From line to point spread function: The general case. *J Opt Soc Am*. 1965;55(4):352. doi:10.1364/JOSA.55.000352
41. van Cittert PH. Zum Einfluß der Spaltbreite auf die Intensitätsverteilung in Spektrallinien. II. *Z Für Phys*. 1931;69(5-6):298-308. doi:10.1007/BF01391351
42. Poppe B, Djouguela A, Blechschmidt A, Willborn K, Rühmann A, Harder D. Spatial resolution of 2D ionization chamber arrays for IMRT dose verification: single-detector size and sampling step width. *Phys Med Biol*. 2007;52(10):2921-2935. doi:10.1088/0031-9155/52/10/019
43. Poppe B, Stelljes TS, Looe HK, Chofor N, Harder D, Willborn K. Performance parameters of a liquid filled ionization chamber array: properties of a liquid filled ionization chamber array. *Med Phys*. 2013;40(8):082106. doi:10.1118/1.4816298
44. Lechner W, Georg D, Palmans H. An analytical formalism for the assessment of dose uncertainties due to positioning uncertainties. *Med Phys*. 2020;47(3):1357-1363. doi:10.1002/mp.13991
45. Sawakuchi GO, Zhu XR, Poenisch F, et al. Experimental characterization of the low-dose envelope of spot scanning proton beams. *Phys Med Biol*. 2010;55(12):3467-3478. doi:10.1088/0031-9155/55/12/013
46. Moignier C, Tromson D, de Marzi L, et al. Development of a synthetic single crystal diamond dosimeter for dose measurement of clinical proton beams. *Phys Med Biol*. 2017;62(13):5417-5439. doi:10.1088/1361-6560/aa70cf
47. Grevillot L, Stock M, Palmans H, et al. Implementation of dosimetry equipment and phantoms at the MedAustron light ion beam therapy facility. *Med Phys*. 2018;45(1):352-369. doi:10.1002/mp.12653
48. Giordanengo S, Manganaro L, Vignati A. Review of technologies and procedures of clinical dosimetry for scanned ion beam radiotherapy. *Phys Med*. 2017;43:79-99. doi:10.1016/j.ejmp.2017.10.013
49. Harms J, Chang C, Zhang R, Lin L. Nuclear halo measurements for accurate prediction of field size factor in a Varian ProBeam proton PBS system. *J Appl Clin Med Phys*. 2020;21(1):197-204. doi:10.1002/acm2.12783
50. McAuley GA, Teran AV, Slater JD, Slater JM, Wroe AJ. Evaluation of the dosimetric properties of a diode detector for small field proton radiosurgery. *J Appl Clin Med Phys*. 2015;16(6):51-64. doi:10.1120/jacmp.v16i6.5391
51. Metzner E, Bäumer C, Behrends C, et al. Spectral fiber dosimetry with beryllium oxide for quality assurance in hadron radiation therapy. *J Instrum*. 2022;17(02):P02009. doi:10.1088/1748-0221/17/02/P02009
52. Delfs B, Blum I, Tekin T, et al. The role of the construction and sensitive volume of compact ionization chambers on the magnetic field-dependent dose response. *Med Phys*. 2021;48(8):4572-4585. doi:10.1002/mp.14994

How to cite this article: Kretschmer J, Brodbek L, Behrends C, et al. Comprehensive investigation of lateral dose profile and output factor measurements in small proton fields from different delivery techniques. *Med Phys*. 2023;50:4546–4561.
https://doi.org/10.1002/mp.16357